2020-01-2098 Published 15 Sep 2020

Internal Diesel Injector Deposit Chemical Speciation and Quantification Using 3D OrbiSIMS and XPS Depth Profiling

Joseph S. Lamb University of Nottingham

Jim Barker and Edward Wilmot Innospec

David J. Scurr, Colin E. Snape, and Emily F. Smith University of Nottingham

Citation: Lamb, J.S., Barker, J., Wilmot, E., Scurr, D.J., et al., "Internal Diesel Injector Deposit Chemical Speciation and Quantification Using 3D OrbiSIMS and XPS Depth Profiling," *SAE Int. J. Advances & Curr. Prac. in Mobility* 3(1):349-364, 2021, doi:10.4271/2020-01-2098.

This article was presented at the SAE Powertrains, Fuels & Lubricants Meeting, Krakow, Poland, Sept. 22-23, 2020.

Abstract

The impact of internal diesel injector deposits (IDIDs) on engine performance, efficiency and emissions remains a major concern in the automotive industry. This has been compounded in recent years by fuel injection equipment developments and changes to diesel fuel towards ultra-low sulfur diesel (ULSD) and biodiesel as well as the introduction of new fuels such as hydrotreated vegetable oil (HVO). Prevention and mitigation of such deposit formation requires an understanding of the formation process, which demands a chemical explanation. The chemistry of these deposits therefore remains a key research interest to the industry using the latest analytical methodologies to inform and build further on previous investigations. In this work, 3D OrbiSIMS analysis using a time of flight-secondary ion mass spectrometer (ToF-SIMS) with hybrid Orbitrap™ functionality has been employed for chemical speciation and depth profiling of IDIDs in-situ on two injector needle samples from field failures in China and Eastern USA. The instrument's soft gas cluster ion beam (GCIB) and high mass resolution enables unequivocal identification of chemistries from several classes of compounds. Here, chemistries identified include alkylbenzene sulfonates, zinc oxides, sodium and calcium salts, carboxylic acids, carbonaceous/polyaromatic hydrocarbons and metal substrate related material. With depth profiling, the distributions of these materials are traced throughout the deposit thickness. Given the semi-quantitative nature of SIMS data, X-ray photoelectron spectroscopy (XPS) depth profiling using an argon GCIB has also been employed to provide parallel data of atomic concentration through the deposit thickness. This data is complementary to SIMS as it places the chemical information in a quantitative context, most notably showing that despite the extreme intensities of salt material in the SIMS data, carbon is the main element throughout both IDIDs. Together the techniques show in general the more functionalized chemistries are at the deposit surface, with underlying salt layers and innermost layers of more amorphous organic material. These techniques represent a new method of comprehensive IDID characterization that affords diagnostic chemical information alongside elemental quantification, thus complementing previous studies.

Introduction

Since the 1980s, deposit control additives (DCAs) have been used to prevent the build-up of deposits in and on diesel fuel injection equipment (FIE) [1]. The deleterious impacts of such deposits on an engine's performance, efficiency and emissions are well documented and in the most extreme cases can result in engine failure [2, 3]. While in the past deposit formation could largely be attributed to imperfect practices that resulted in fuel contamination, incorrect additivation or adulteration [4], these recent reports are believed to arise from a series of rapid changes in the automotive and fuels industries, driven primarily by legislation as governments respond to the climate crisis with more stringent emissions and renewable fuels policies [5]. Fuel has moved towards ultra-low sulfur diesel (ULSD) and renewable fuel blends using biodiesel and hydrogenated vegetable oil (HVO), a newer fuel that is highly paraffinic. While a link between biodiesel's fatty acid methyl esters (FAME) and deposits has been established [6], HVO's relationship to IDIDs is inconclusive, though in engine testing a pure HVO fuel has shown a higher tendency to block the injector than traditional rapeseed methyl ester (RME) biodiesel [7]. FIE developments, namely high pressure common rail technology (HPCR), have led to higher injection pressures and temperatures, as well as more intricate designs with more exacting tolerances that are particularly vulnerable to, and negatively affected by, deposit formation [5]. Certain additives have been linked to IDID formation, such as dodecenylsuccinic acid (DDSA) [5, 7, 8], which is believed to react with sodium. It is expected that injector deposits will continue to become more common and severe, as injection pressures continue to increase to meet further targets [9].

Understanding the source of chemistries in engine deposits is an essential step towards developing prevention and mitigation strategies. Previous IDID research is extensive and has applied a multitude of techniques [9] including scanning electron microscopy-energy dispersive x-ray spectroscopy (SEM-EDS) [6, 10, 11], transmission electron microscopy (TEM) [12, 13], Fourier transform infra-red spectroscopy (FTIR) [14, 15, 16], time of flight-secondary ion mass spectrometry (ToF-SIMS) [2, 10, 17, 18] and X-ray photoelectron spectroscopy (XPS) [10, 13]. These techniques have afforded much chemical and structural information, but analysis is not trivial due to the rough topography, layering of chemistries and the range of chemistries observed, from salts and soaps to lacquers and carbonaceous material [12].

Towards probing the sub-surface chemistry of these layered structures, ToF-SIMS has been a technique of great interest based on its ability to chemically interrogate samples with depth while preserving deposit provenance. Previously, Barker *et al.* have applied ToF-SIMS to an IDID which provided chemical information as a function of depth and revealed layering of chemistries, however this information was limited to single elements and small organic and salt fragments such as C_3N^-, C_6^- and S^- [2, 17]. Dallanegra and Caprotti also performed elemental ToF-SIMS profiling using a Cs^+ beam on needle IDIDs from engine tests, revealing layering effects consisting of an outer organic film above an oxide layer which interfaced with the needle's metal surface [10].

XPS is a technique favored for accurate determination of the relative atomic percentages of almost all elements excluding hydrogen. With modelling of bonding components, it can also quantify the types of bonding present. Previous investigations into diesel injector deposits are limited to the deposit surface. Venkataraman *et al.* observed only carbon and oxygen in a respective ratio of 84:16 [13] and Dallanegra and Caprotti also found carbon to dominate the spectra (77.8–78%) with smaller amounts of nitrogen and oxygen and traces of sodium, copper, zinc, sulfur and chlorine [10].

This work is a development on the ToF-SIMS method utilizing 3D OrbiSIMS analysis with the Hybrid SIMS (IONTOF GmbH) instrument, providing improved mass resolution and softer sputtering with the $Ar_{2300-3000}^+$ cluster GCIB [19]. We have recently demonstrated the advantages 3D OrbiSIMS can provide in engine deposit analysis, comparing results from an IDID, a gasoline direct injection (GDI) injector deposit and a diesel filter [20]. Here, dynamic SIMS runs were carried out from which chemical structures were assigned, with their intensities seen as a function of depth. In view of SIMS' semi-quantitative nature and its propensity to give the impression of false significance to certain highly ionizable fragments, XPS depth profiling was employed as a quantitative "grounding", providing parallel atomic percentage depth profile data that can contextualize and substantiate the SIMS data.

The structure of this paper begins with SEM-EDS data to demonstrate deposit morphology and provide an idea of the elements present. In the 3D OrbiSIMS spectra, chemical information is then probed and the two samples compared. From the depth profiles, the distribution of these chemistries through the deposit depth is examined to reveal the IDIDs' chemical layering. Finally, XPS depth profile data quantifies the elemental composition of the sub-surface deposit material as a bulk and as a function of depth.

Methodology

Samples

Two injector needle samples from failed field diesel injector systems were analyzed. Needle 1 (Figure 1a) originates from China and Needle 2 (Figure 1b) originates from Eastern USA with reported complaints of a stuck injector preventing vehicle start. Both samples present visual discoloration due to deposit, particularly towards the needle tips, which was hence where analysis was performed with all techniques (blue in Figure 1) under the assumption that the deposit material is consistent and directly comparable across this region.

SEM-EDS Experimental

SEM was used to provide visual detail of the deposit material and give an overview of deposit distribution and morphology. Additionally, to avoid ambiguity in XPS and aid with assigning SIMS data, EDS was used to identify the main elements in each sample.

A Thermo Scientific FEI Quanta 600 ESEM (Thermo Fisher Scientific Inc.) instrument equipped with a Bruker Nano XFlash series EDS detector was used with low vacuum (60 Pa) and an accelerating voltage of 20 kV. Backscatter images are displayed as they provide more information about the samples.

3D OrbiSIMS Experimental

The samples were analyzed using the Hybrid SIMS instrument for dynamic high-resolution 3D OrbiSIMS depth profiling (mode 4 as described by Passarelli *et al.* [19]). The primary ion source was a 20 kV GCIB with clusters of $Ar_{2300-3000}^+$ and 200 × 200 µm sputter area. The Orbitrap™ analyzer was used, providing 240,000 mass resolution at 200 *m/z*. An *m/z* range of 75–1125 rather than 150–2250 was found to be more useful

FIGURE 1 Optical microscope image of a) Needle 1 (origin China) and b) Needle 2 (Eastern USA), showing analysis areas in blue.

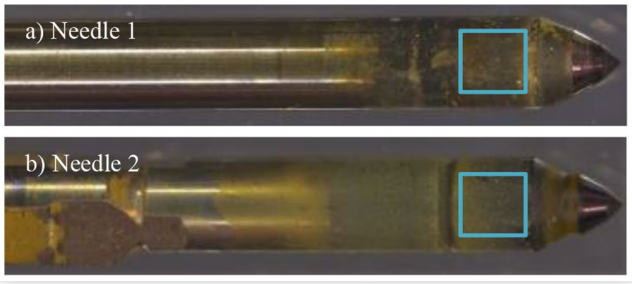

as there is data of interest in the 75–150 range and little in the 1125–2250 range. However, the negative polarity 150–2250 *m/z* data is displayed for the depth profile of Needle 1 as this profile was run for longer. The data was analyzed and processed using SurfaceLab 7 (IONTOF GmbH). Spectra were exported with no binning and depth profiles were exported using a running average of 1000 data points for clarity and plotted with a sixth order polynomial fitting. All ions' intensities are normalized to the total spectrum areas which were estimated using the trapezoidal rule. All SIMS assignments' deviations are ≤ 2.5, with some exceptions below 90 *m/z* where a threshold of ≤ 4 is used as Orbitrap™ analyzers are less accurate in this range. Uncertain assignments were confirmed by analysis of isotopic patterns or using the Hybrid SIMS' MS/MS function whereby a certain ion can be isolated, further fragmented and its own fragments analyzed.

XPS Experimental

XPS data was acquired with a Kratos AXIS ULTRA DLD instrument using a monochromated Al Kα ($h\nu$ = 1486.6 eV) X-ray source in electrostatic mode with a small (110 µm) aperture. The optical camera was used for height optimization as electrostatic mode does not allow height optimization using the electron lenses. The depth profile was performed using an Ar_{500}^+ GCIB at 20 kV. A large etch area (around 1mm) was used to provide a buffer zone, ensuring the analysis area would align within the etch crater. Etch times between measurements varied, with longer etches (up to 5 minutes) towards the ends of the runs. The total etch time was 2725 s for Needle 1 and 5700 s for Needle 2. Charge neutralization was applied with 2.0 A filament current, a balance plate voltage of 3.6 V and a bias of 1.2 V. High resolution spectra were collected for the oxygen 1s peak (527-539 eV binding energy) for the depth profile.

CasaXPS Version 2.3.22PR1.0 (Casa Software Ltd) was used to process and interpret the XPS data. The values for each element were referenced to the XPS reference pages of XPSFitting [21]. Both regions and components were fitted using linear backgrounds, and a GL(30) lineshape (70% Gaussian with 30% Lorentzian curve) was used for fitting components. For determining atomic percentages, Relative Sensitivity Factors (RSF) from the Kratos library (RSF of F 1s = 1) were used. Profiles were plotted using a sixth order polynomial fitting to demonstrate the trends, with error bars plotted using Monte Carlo uncertainty values calculated by the CasaXPS software.

Results and Discussion

SEM-EDS for Morphology and Elemental Information

SEM-EDS analysis was performed on the two IDID samples (shown in Figure 2a, 2b and Table 1) to establish an idea of deposit morphology and elemental composition. In the SEM images, Needle 1 is observed with more heterogeneity, while both show rough topography similar to the appearances seen in previous fouled injector needle investigations [6, 11]. Digital contrast and brightness enhancements were applied to the image of Needle 2.

EDS results are shown in Table 2. Values are not quoted due to the semi-quantitative nature of EDS, with XPS instead being used for quantification. The substrate elements seen are standard alloying metals and are the same across the two samples, and the deposit elemental composition is consistent with the content of diesel fuel, diesel and engine lubricant additives and common salt contaminants. The most notable difference is the presence of zinc and phosphorus on Needle 1, which suggests a zinc dialkyldithiophosphate (ZDDP) contamination in the injector.

FIGURE 2 a) SEM backscattered electron image of Needle 1 at ×34 magnification, b) SEM backscattered electron image of Needle 2 at ×18 magnification with digital contrast and brightness enhancement.

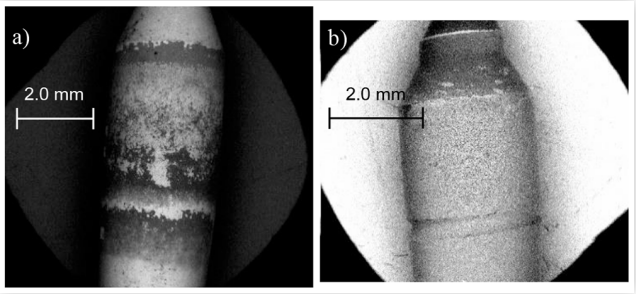

TABLE 1 EDS results

Sample	Deposit	Substrate
Needle 1	C, O, N, Na, Ca, S, P, Si, Zn	Fe, Cr, Mo, W, V, Al
Needle 2	C, O, N, Na, Ca, S, Cl, K	Fe, Cr, Mo, W, V, Al

TABLE 2 Elemental composition (atomic percentage) with standard deviation for each sample from the summed XPS spectra in Figure 8, excluding iron, chromium and molybdenum (metal substrate elements seen in Needle 1)

	Needle 1		Needle 2	
Element /Orbital	At %	σ	At %	σ
C 1s	68.9	0.2	61.4	0.3
O 1s	19.9	0.1	15.2	0.2
N 1s	2.5	0.2	7.5	0.2
Na 1s	0.4	0.04	11.1	0.1
Ca 2p	5.9	0.06	0.3	0.05
Cl 2p	0	N/A	4.0	0.05
S 2p	0.4	0.04	0.4	0.04
P 2p	0.1	0.02	0	N/A
Zn 2p	1.6	0.3	0	N/A
Si 2s	0.3	0.05	0	N/A

3D OrbiSIMS for Chemical Speciation and Depth Distribution

Overview of Spectra at 75–275 m/z 3D OrbiSIMS analysis was performed on the two samples as described in the experimental in the methodology in order to assess the detailed chemistries of the deposits and their distributions with depth. As the SIMS spectral data is complex and extensive, analysis here is focused on identifying the markers of different types of chemistries with significant ion intensities. Sections of the positive and negative polarity spectra of both needles are shown in Figure 3, with a mass range of 75–1125 *m/z* used as this is most representative of the datasets and their differences. Broken axes are used due to the obfuscation of smaller peaks by certain dominating ions of very high intensities, which are calcium and sodium salt material ($Ca_2O_xH_y^+$ in Needle 1; Na_2Cl^+, $Na_3SO_4^+$ and $NaCl_2^-$ in Needle 2) and a carbon fragment (C_8^- in Needle 1). From SIMS, it cannot be known if this is a genuine quantitative representation of the sample composition or a result of these materials' advanced ionizabilities.

Assessing the dominant peaks at this scale in Figure 3, the spectra show significant fundamental differences that indicate the compositional differences of each IDID. In negative mode, Needle 1 is dominated by a series of carbon fragments (C_8^- to C_{21}^- and smaller intensities of C_8H^- to $C_{18}H^-$), carbon-nitrogen fragments (C_7N^-, C_9N^-) as well as some metal substrate-related oxides (FeO_2^-, CrO_3^-, $VO_4H_2^-$) and salt-related material (PO_3^-, $CaC_3N_3^-$). In contrast, Needle 2 is dominated in negative mode by sodium chloride and sulfate salts ($NaCl_2^-$ to $Na_4Cl_5^-$, $NaSO_4^-$, $Na_2S_2O_8^-$), some of which are mixed within the same ions ($Na_2ClSO_4^-$ to $Na_3Cl_2SO_4^-$) with smaller intensities of sodium cyanates ($NaC_2N_2O_2^-$) and carbon fragments (C_8^- to C_{14}^-). In positive mode, Needle 1's calcium salt material dominates in the form of hydroxides and phosphates ($Ca_2O_2H^+$ to $Ca_3O_7H_9^+$, $CaPO_2^+$ and $Ca_2PO_8H_8^+$) and there is an intense series of substrate-metal hydroxides ($FeO_6H_6^+$ to $Fe_3O_7H_8^+$, $Mn_2O_3H_6^+$ and $Al_2VO_3H_2^+$). Needle 2 shows a wide variety of positive sodium salts including chlorides (Na_2Cl^+ to $Na_5Cl_4^+$), sulfates (Na_3S^+, $Na_3SO_3^+$), carbonate ($Na_3CO_3^+$), cyanate (Na_2CNO^+) and hydroxide ($Na_3O_2H_2^+$). There are also mixed salts ($Na_2CaPO_3H_2^+$, $Na_4SO_4OH^+$ and $Na_4SO_4Cl^+$) with high intensities.

Comparisons of Chemistries Observed in Full Spectra This section consists of a more in-depth account of the chemistries of interest found in each sample from the 75–1125 *m/z* profiles along with examples, including those with weaker signals not visible on the spectra in Figure 3. A tabulated summary of key examples of these types of chemistries along with deviations and normalized intensities can be found in Appendices 1 and 2.

Salt

In negative polarity, Needle 2's most intense salt peaks are 2 orders of magnitude larger than those of Needle 1. Needle 1 shows mostly calcium salts in the form of cyanides ($CaC_3N_3^-$), hydroxides ($CaO_3H_3^-$ to $Ca_3O_7H_7^-$), cyanates ($CaC_3N_3O^-$) and sulfates ($CaSO_4H^-$, $CaSO_4^-$). It also shows smaller intensities of calcium chlorides as well as sodium hydroxides ($NaO_3H_4^-$) and sulfates ($NaSO_4^-$), with much of the chemistry existing mixed within the same ion fragments ($CaC_2N_2Cl^-$, $Ca_2C_3N_3O_2H_2^-$, $CaSO_4CN^-$). This mixing of the anions shows agglomeration within the deposit rather than separation by distinct salt chemistries, though the minimal cation mixing suggests calcium salts and sodium salts are largely separated. Needle 2's most intense negative salt peaks are primarily sodium salts of chloride ($NaCl_2^-$ to $Na_{13}Cl_{15}^-$), sulfate ($NaSO_4^-$ to $Na_9S_5O_{20}^-$), cyanide ($Na_2C_3N_3^-$) and cyanate ($NaC_2N_2O_2^-$). There are smaller amounts of sodium hydroxides as well as calcium cyanides, chlorides and sulfates, which are mostly seen as mixed chemistries ($NaCaSO_4O_2H_2^-$, $CaCNCl_2^-$, $Na_3SO_4CNCl^-$ and $CaSO_4CN^-$). This sample shows more anion and cation mixing, suggesting more salt agglomeration.

The positive polarity data shows similar salt chemistries but unlike the negative data both samples show similar intensity contributions from salt material. As was seen in negative mode, Needle 1 shows intense calcium hydroxide ($Ca_2O_2H^+$ to $Ca_{14}O_{26}H_{22}^+$) and cyanate containing ($Ca_2O_2H_2CNO^+$) peaks, and weaker sodium sulfates ($Na_3SO_4^+$), cyanides ($Na_4CNSO_4^+$) and cyanates ($Na_3C_2N_2O_2^+$). Salt anions exclusive to positive mode are high intensities of calcium phosphates ($CaPO_2^+$ to $CaPO_8H_8^+$) and a low intensity of sodium carbonate ($Na_3CO_3^+$). In Needle 2, there are intense series of peaks from sodium chlorides (Na_2Cl^+ to $Na_{12}Cl_{11}^+$), sulfates (Na_3S^+, $Na_3SO_4^+$ to $Na_9S_4O_{16}^+$), cyanates (Na_2CNO^+, $Na_3C_2N_2O_2^+$) and hydroxides ($Na_3O_2H_2^+$ to $Na_5O_4H_4^+$), and weaker peaks from cyanides (Na_3CNCl^+ to $Na_8CNCl_6^+$). Calcium hydroxides also appear in Needle 2's positive data with small intensities ($Ca_2O_3H_3^+$ to $Ca_4O_8H_9$) as well as much smaller intensities of calcium chlorides and sulfates which are seen in mixed salts ($CaNa_2SO_4OH^+$, $CaNa_3SO_4ClOH^+$). Intense sodium carbonates appear in the positive data with high intensity ($Na_3CO_3^+$), however phosphate is absent, correlating with the absence of phosphorus in Needle 2's EDS data. Potassium salts also appear in Needle 2's positive data as intense chlorides (K_2Cl^+) and mixed ions with sodium in chlorides ($KNaCl^+$) and sulfates ($KNa_2SO_4^+$).

This wide variety of salt material identified may represent a number of sources with prime suspects being storage tank bottoms, refinery polishing, barge transportation, lubricant oil contamination or poor quality biodiesel as has been previously documented [15]. The major known sources of calcium are lubricating oil and poor-quality biofuel, and its presence with sulfates and phosphates indicates the former origin as these are components of lubricant additives. Further evidence of lubricant additives is seen, with alkylbenzene sulfonates (ABS) in Needle 2 and both ABS and zinc in Needle 1. The range of anions seen and their co-existence is evidence of the complexity of reaction and degradation mechanisms at play in the diesel engine.

FIGURE 3 3D OrbiSIMS spectra showing *m/z* range 75–275 of a) Needle 1 in negative polarity (1.4 hr run time), b) Needle 2 in negative polarity (14.7 hr tun time), c) Needle 1 in positive polarity (18.1 hr run time), and d) Needle 2 in positive polarity (13.1 hr run time). All spectra are normalized to the respective total ion count of the full mass range spectrum (75–1125 *m/z*).

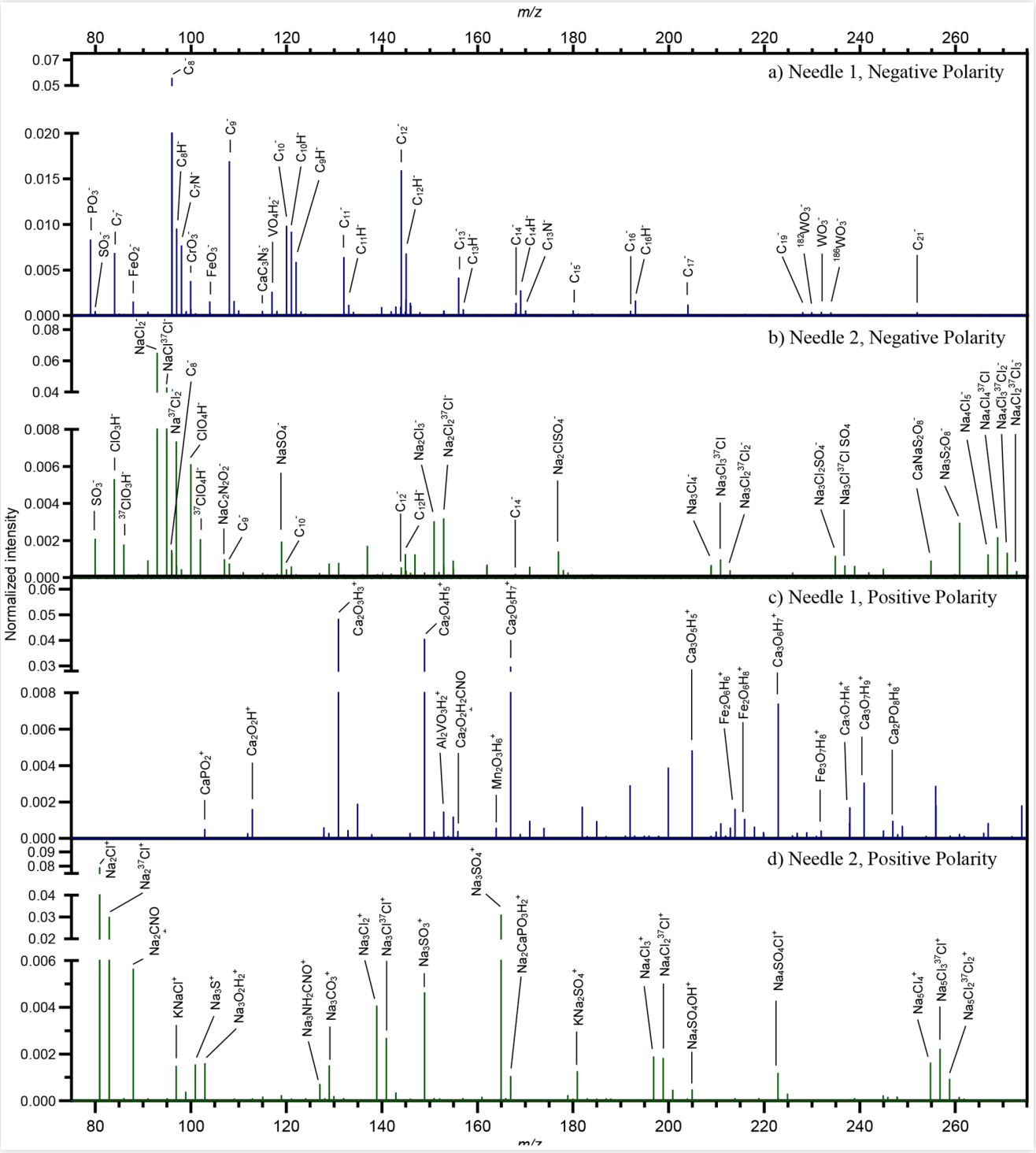

Carbonaceous/Hydrocarbon

As would be predicted from the majorly hydrocarbon composition of diesel, both samples feature carbonaceous and hydrocarbon ions with large intensities, primarily as carbon fragments and as hydrocarbons where nC > nH. The ions' high carbon content relative to hydrogen may imply any combination of three origins:

1. Sputtered fragments of organic material that lose hydrogen atoms and potentially other elements during bombardment with the ion beam

2. Polyunsaturated hydrocarbons or polycyclic aromatic hydrocarbons (PAHs) (soot-like content)
3. A possible diamond-like carbon (DLC) substrate protective coating that can be placed on an injector needle by the manufacturer [22].

In negative polarity, the most intense carbonaceous/hydrocarbon ions in both samples are carbon fragments in a homogenous series from C_7^- to C_{25}^- in Needle 2 and to C_{35}^- in Needle 1, which are more intense in Needle 1 by around 2 orders of magnitude. There is a similar, lower intensity series of C_7H^- to $C_{20}H^-$ in Needle 2 and $C_{27}H^-$ in Needle 1, which are around an order of magnitude higher intensity in Needle 1. Both samples contain large intensities of $C_xH_y^-$ hydrocarbon fragments with $x < 20$ and $y < 10$. These are generally higher intensities in Needle 1, however Needle 2's data is more distributed towards these more hydrogen rich ions while Needle 1 is dominated by the carbon fragment ions. This indicates more unsaturated/polycyclic aromatic hydrocarbon (PAH) content in Needle 1, which could be a sign of a longer residence time of the deposit on the needle or of harsher FIE conditions.

In positive polarity, Needle 2's highest intensity hydrocarbon ions ($C_9H_7^+$, $C_{10}H_8^+$) are an order of magnitude greater than those of Needle 1 ($C_9H_7^+$, $C_{12}H_8^+$), with many of these representing (polycyclic) aromatic formulae such as naphthalene and acenaphthylene. This contrasts with negative mode where Needle 1 had higher intensity carbonaceous/hydrocarbon ions, and is likely a result of the hydrogen-rich ions characterizing Needle 2 being more ionizable in positive mode, while the less H-saturated ions prevalent in Needle 1 are more ionizable in negative mode. The distribution of these ions in Needle 1 tends towards larger ions including peaks for $C_{41}H_{17}^+$, $C_{38}H_{16}^+$, $C_{56}H_{20}^+$ and $C_{39}H_{15}^+$ which are absent in Needle 2 and again point towards increased PAH content in Needle 1. Needle 2 has a more intense (1 order of magnitude) positive carbon fragment homologous series (C_x^+ where in Needle 1 x=8-31 and in Needle 2 x=10-23) which appears to oppose the negative data that showed Needle 2 trended towards more hydrogen-rich ions. However, it is seen in the depth profile that in Needle 2 these are exclusively associated with the lowermost layer. Hence, the carbonaceous/hydrocarbon data points towards a more amorphous content in the bulk deposit of Needle 1, while Needle 2 has more hydrogen saturation in this region but an amorphous, possible DLC substrate carbon content in the lowermost layer seen in positive ionization.

Nitrogenous

Nitrogen-containing additives are used with diesel fuel, such as 2-ethylhexyl nitrate (2-EHN), a cetane number improver that, if breakdown occurs in the fuel, is known to affect fuel stability [23, 24]. Nitrogen-containing compounds are also a component of crude oil and a small amount are present in the final diesel fuel, which can be destabilizing compounds such as pyrroles, pyridines, quinolines and indoles [25].

In the negative data, there is a series of nitrogenous C_xN^- fragments (x=6-22 in Needle 1, x=6-14 in Needle 2) with intensities 1-2 orders of magnitude higher in Needle 1 than Needle 2, a similar trend to the C_x^- carbon fragments. Needle 2's data is distributed more towards hydrogen-containing fragments such as $C_xNH_4^-$ and $C_xNH_6^-$ where x=8-14, indicating a lower hydrogen content in Needle 1, likely due to a higher nitrogen containing polycyclic aromatic compound (NPAC) or soot-like content, similarly to the carbonaceous PAH data.

There are assignments in the positive data corresponding to structures such as indole ($C_8H_7N^+$) and quinaldine ($C_{10}H_9N^+$) which are present in both samples but more intense in Needle 2 (1 order of magnitude). There are also fragments that may correspond to structures that have undergone deprotonation during sputtering such as 2-methylindole ($C_9H_8N^+$) and, again, quinaldine ($C_{10}H_8N^+$) which are also more intense in Needle 2. Deprotonation is a common process during particle bombardment and is likely to occur during SIMS measurements [26]. As with the carbonaceous and hydrocarbon data, the positive data contrasts with the negative as Needle 2 has assignments with intensities an order of magnitude higher than Needle 1. These ion masses are slightly larger in Needle 1, though C/H ratios are very similar as exemplified by the most prevalent ions in Needle 1 being $C_{11}H_8N^+$ and $C_{12}H_{14}N^+$ and in Needle 2 being $C_9H_8N^+$ and $C_8H_7N^+$.

Needle 2 also has more intense peaks (1-2 orders of magnitude in both polarities) for ions containing two nitrogen atoms such as $C_5N_2H^-$ and $C_7N_2H^-$ in negative mode and $C_5H_7N_2^+$ and $C_8H_9N_2^+$ in positive mode, suggesting again a more complex, functionalized chemistry in this sample.

Oxygenates

Oxygenates are another often destabilizing class of compounds found in crude oil and in smaller amounts in diesel fuel, some of which are thought to reduce fuel stability such as phenols and peroxides [27]. The esters in biodiesel are another potential source of oxygen in deposits, as they are known to decompose to carboxylic acids that can form soaps [15]. Oxygen-containing additives such as 2-EHN can also be a source of oxygen.

Oxygenate intensities in the negative data are slightly stronger in Needle 2, and are distributed slightly towards larger fragments with a higher hydrogen content, exemplified by the two largest intensity ions in Needle 2 ($C_8H_5O^-$ and C_6OH^-) and in Needle 1 (C_6OH^- and C_8O^-). This data shows a similar phenomenon to the nitrogenous material whereby Needle 2's ions are more hydrogen saturated. In positive mode, Needle 2 again has higher intensity peaks (1 order of magnitude) but Needle 1 has higher mass, less hydrogen-rich ion fragments. Like with nitrogenous material, there are oxygenates that may relate to aromatics that are prevalent in both samples, such as a dehydrogenated acetophenone ($C_8H_7O^+$) and dibenzofuran ($C_{12}H_8O^+$).

There are ions with formulae matching stearate and palmitate ($C_{18}H_{35}O_2^-$ and $C_{16}H_{31}O_2^-$) in Needle 1's negative spectrum that are not seen Needle 2. These are some of the most common fatty acids in nature, and have been seen in previous deposits [11, 18]. Their origin may be from biodiesel, where they are commonly seen alongside other fatty acid chain lengths [28], however it is possible that they result from surface contamination of the sample.

FIGURE 4 Highest intensity ABS ions seen in both samples' negative mode spectra

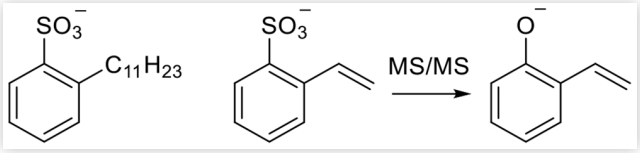

Alkylbenzene Sulfonates (ABS)

ABS compounds are detergent molecules used as lubricant additives [29]. Often, they are accompanied by calcium counter-ions, and calcium has been observed in both samples' salt material along with sulfate anions. As lubricant additives, they should not be found on or in FIE and their presence suggests lubricant oil adulteration or contamination. A series of ABS compounds ($C_8H_7SO_3^-$, $C_9H_9SO_3^-$ $C_{17}H_{27}SO_3^-$, $C_{19}H_{31}SO_3^-$) are seen in both samples, with a similar distribution seen for both samples in which $C_8H_7SO_3^-$ is the most prominent ion. Using the Hybrid SIMS' tandem mass spectrometry (MS/MS) functionality on the $C_8H_7SO_3^-$ ion, it was found to fragment into $C_8H_7O^-$ and SO_3^-. $C_8H_7O^-$ has a comparable intensity to $C_8H_7SO_3^-$ in both samples and corresponds to the phenolate form (Figure 4), which has been reported to form in the gas phase from a rearrangement of alkylbenzene sulfonates [30].

Zinc

Zinc is known to contribute towards deposits to such an extent that its introduction to fuel as zinc neodecanoate forms the standardized engine test (CEC F-98-08) for simulation of injector deposit formation [31]. Zinc is not a component or additive of diesel fuel but may emerge as an impurity due to zinc-containing tanks, possible zinc-coatings on injector components or the anti-wear lubricant oil additive zinc dialkyldithiophosphates (ZDDP) (Figure 5) [29, 31]. Contamination from the injector is unlikely as Needle 1's metal substrate was shown using EDS to not contain zinc, while the presence of other lubricant oil associated chemistries in this sample (ABS compounds, phosphates and calcium) is evidence of lubricant oil contamination.

As with EDS, in the 3D OrbiSIMS data zinc is present only in Needle 1. It is seen as an oxide (ZnO_2^-) and a sulfinyl ($ZnSO^-$), which both exhibit zinc's isotope pattern. The presence of sulfur with this sample's zinc supports ZDDP contamination, though these ions suggest a decomposition of the complex and oxidation of the zinc. Lubricant oil has been identified in the past as a contributor towards deposits [4], with zinc suggested to act as a catalyst, form fatty acid soaps, or precipitate out as zinc oxide [24]. The presence of zinc oxide in this deposit suggests the latter mechanism. The origin of a lubricant oil injector contamination may be adulteration of the fuel, leakage within the engine or backwards flow into the FIE of combustion products containing lubricant oil from cylinder lubrication and blow-by gases.

FIGURE 5 ZDDP structure

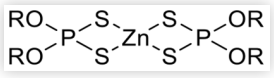

Polydimethylsulfoxane (PDMS)

PDMS is a known common contaminant of sample surfaces however is also used as an anti-foaming additive in diesel fuel [23]. A PDMS marker ($Si_2O_2C_4H_{13}^+$) is seen with high intensity in Needle 1's positive data, while no evidence can be found on Needle 2. This implies either a larger surface contamination in the handling of Needle 1, or a surface deposition of this additive from the fuel. PDMS has been identified as part of an IDID before using ToF-SIMS, though an origin was not explored [18].

Needle Substrate Metals

Needle 2 has a notable lack of metal substrate-related fragments limited to weak peaks of iron and chromium, while Needle 1 has an intense series of iron, chromium, tungsten, vanadium and molybdenum oxides that, in accordance with the EDS data, indicate the metal substrate. These are found in both negative (CrO_3^-, FeO_2^-, FeO_3^-, MoO_3^-, MoO_4^-, WO_3^-, VO_3^-) and positive ($Fe_2O_6H_6^+$, $Fe_2O_6H_8^+$, $Fe_3O_7H_8^+$, $MoO_3H_2^+$, $Mo_2O_7H_8^+$, $Mo_2O_6H_7^+$) polarities, and these ions are generally 3 or more orders of magnitude larger in Needle 1 than in Needle 2 or are entirely absent in Needle 2.

3D OrbiSIMS Depth Profiling to Probe Chemical Distribution

Positive and negative polarity depth profiles for Needle 1 and Needle 2 were collected to demonstrate the distribution of chemistry throughout each deposit thickness (Figures 6 and 7). On each profile, key ions are displayed for the sample to demonstrate its chemical trends. The negative polarity profile for Needle 1 is for mass range 150-2250 m/z while the others are for 75-1125 m/z. The profiles displayed are cut at 50,000 s (13.9 hours) for Needle 1 and 30,000 s (8.3 hours) for Needle 2 as all respective ions had reached final plateaus at these points.

Needle 1 3D OrbiSIMS Depth Profile

Both the negative (Figure 6a) and positive (Figure 6b) polarity depth profiles for Needle 1 show agreement in layering effects. Carbonaceous material ($C_{14}H^-$, C_{17}^-) is the most intense chemistry throughout Needle 1's negative mode depth profile, which loses intensity more quickly near the surface but steadily throughout while metals rise (WO_3^-, MoO_4^-; note that FeO_3^- and CrO_3^- are excluded due to the mass range). The other carbonaceous ion (the hydrocarbon $C_{17}H_5^-$) obeys the same pattern, but with a much lower intensity. The nitrogenous fragments ($C_{13}N^-$ and $C_{14}NH_4^-$) and salt material ($Ca_2O_5H_5^-$, $Ca_3O_7H_7^-$, $Ca_2C_3N_3O_2H_2^-$) also follow the same

FIGURE 6 Needle 1 3D OrbiSIMS depth profiles in a) Negative polarity and b) Positive polarity

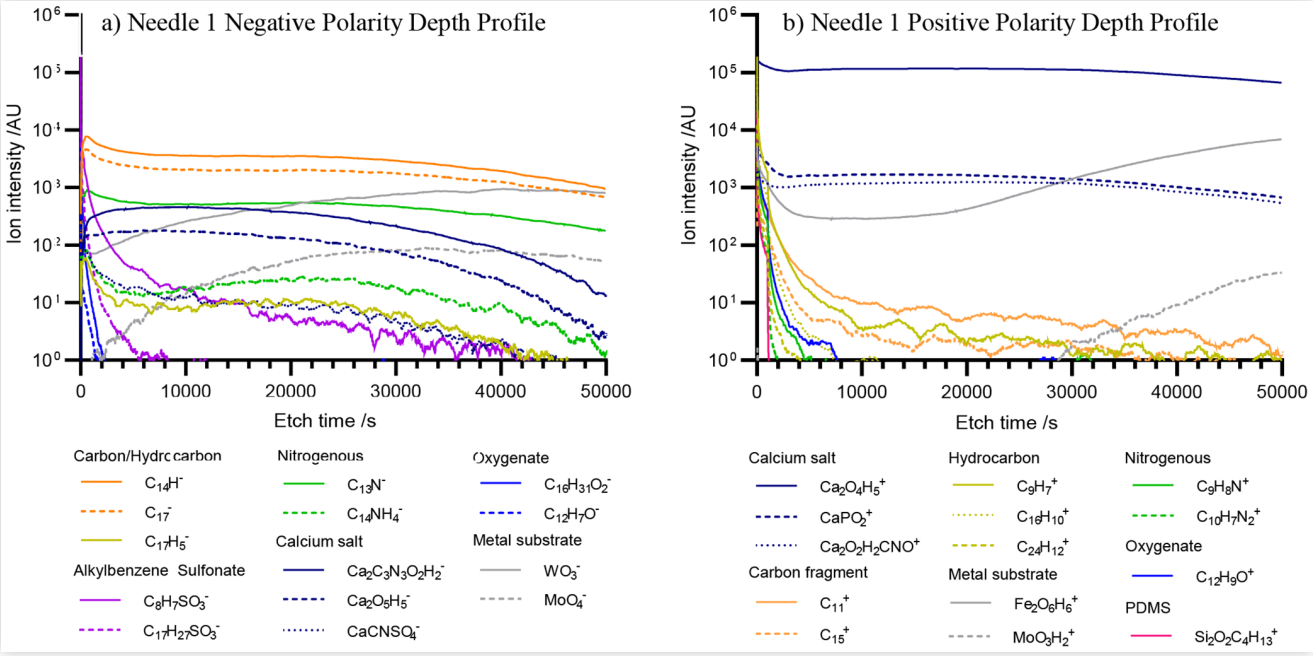

FIGURE 7 Needle 2 3D OrbiSIMS depth profiles in a) Negative polarity and b) Positive polarity

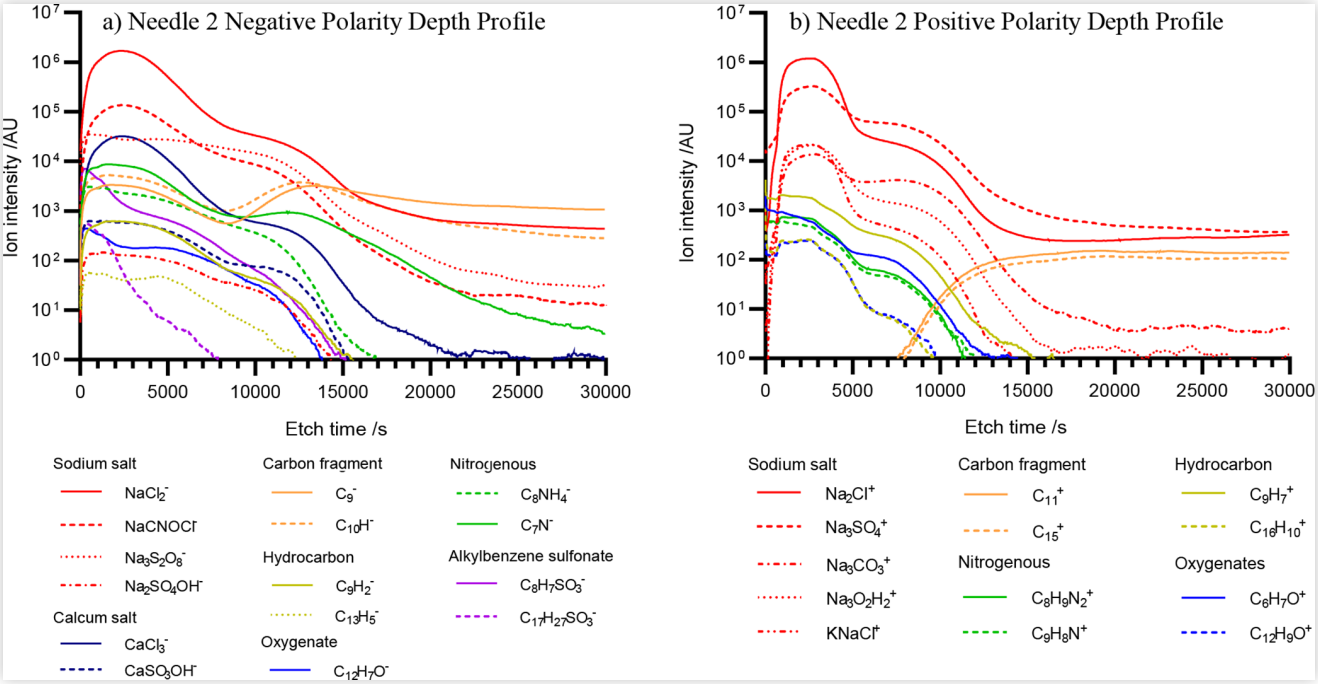

trend of a steady decline throughout, though the more hydrogen-rich nitrogenous material and the calcium sulfate show a sharper decline near the surface.

In positive polarity, the calcium salt ions ($Ca_2O_4H_5^+$, $CaPO_2^+$, $Ca_2O_2H_2CNO^+$) follow this same trend and are the highest intensity type of material throughout. Again, metal substrate ions ($Fe_2O_6H_6^+$, $MoO_3H_2^+$) show a gradual rise throughout most of the profile, however $Fe_2O_6H_6^+$ is seen with a high surface intensity and initial fall until around 200 s before this rise, likely a result of either wear metal from the engine or metal traces left on the needle surface caused by removal from its housing.

Another trend in the data is that of ions with significant intensity only towards the surface (<20000 s etching). In negative mode this comprises only ABS fragments ($C_8H_7SO_3^-$, $C_{17}H_{27}SO_3^-$) and oxygenates ($C_{16}H_{31}O_2^-$, $C_{12}H_7O^-$) while in positive mode there are carbon fragments (C_{11}^+, C_{15}^+), hydrocarbons ($C_9H_7^+$, $C_{24}H_{12}^+$), oxygenates ($C_{12}H_9O^+$) and

nitrogenous fragments ($C_9H_8N^+$, $C_{10}H_7N_2^+$). For each of these classes of ion, the larger, more complex fragments fall away sooner than the simpler fragments. This implies a breakdown of complex chemistries over the time resident in the deposit.

The oxygenates in negative mode, as well as PDMS in positive mode ($Si_2O_2C_4H_{13}^+$) show the most precipitous declines, falling to noise after around 2000 s. Palmitate ($C_{16}H_{31}O_2^-$) and stearate ($C_{18}H_{35}O_2^-$) are both seen with sharp near-surface declines. This suggests these materials arise from either surface contamination or deposition on a pre-formed deposit. PDMS and palmitic acid have been seen together in previous ToF-SIMS analysis of a needle shaft IDID [18].

Needle 2 3D OrbiSIMS Depth Profile

Needle 2's positive (Figure 7a) and negative (Figure 7b) polarity depth profiles show more dramatic layering effects than Needle 1's and show trends that mostly agree with one another.

Both polarities highlight the large intensity of salt material, with an initial steep rise at the surface to a salt-dominated layer, followed by a decline with a temporary plateau at an interface with a carbon fragment layer. The negative polarity profile shows that both sodium salts ($NaCl_2^-$, $NaCNOCl^-$, $Na_3S_2O_8^-$, $Na_2SO_4OH^-$) and calcium salts ($CaCl_3^-$, $CaSO_3OH^-$) follow the same profile trend. Chloride, hydroxide, sulfate and cyanate salts all follow roughly this same pattern, though sulfates appear less prevalent in the initial sub-surface salt layer, showing a flatter profile in this region. The positive data shows the same trend line for salt (Na_2Cl^+, $Na_3SO_4^+$, $Na_3O_2H_2^+$, $Na_3CO_3^+$, $KNaCl^+$) and the same relative lack of sulfate in the sub-surface layer, with carbonate also weaker in this layer. Potassium salts are present mostly mixed with sodium, and here can be seen following the same profile pattern as sodium and calcium salts.

In negative mode, the carbon fragments (C_9^- and $C_{10}H^-$) initially follow a similar pattern to the salt material with a rise and subsequent fall after around 2500 **s** etch time. However, at a final interface beginning at 10,000 s, these ions rise again while salt continues to decline. Carbon then remains the most intense material for the remainder of the profile. This behavior relates to etching having reached a resistant layer of either DLC or hardened carbonaceous deposit material. The C_x^- and C_xH^- fragments are generally seen throughout the profile, with the exception of some C_xH^- fragments where x=7, 9, 11, and $\geq$ 23 which fall to noise at this final salt-carbonaceous interface, alongside the more hydrogen saturated hydrocarbon ions ($C_9H_2^-$, $C_{13}H_5^-$). In the positive data, the carbon fragments (C_{11}^+ and C_{15}^+) are absent until the final interface, again at around 10,000 s, and are intense from here onwards. Salt ions remain the most intense, though this is most likely due to their higher ionizability. In contrast with the carbon fragments in the negative data and in Needle 1's negative and positive data, these C_x^+ ions are exclusive to the lowest carbon layer, with the exception of C_{16}^+ and $C_{21\text{-}23}^+$, which have a brief presence towards the surface.

Much of the chemistry in both positive and negative modes follows a common trend of a slow decline that accelerates at around 8000 s or, for more complex or larger ions, follows this same shape but with a steeper, earlier decline. This includes hydrocarbon ($C_9H_2^-$, $C_{13}H_5^-$, $C_9H_7^+$, $C_{16}H_{10}^+$), oxygenate ($C_{12}H_7O^-$, $C_8H_7O^+$, $C_{12}H_9O^+$), nitrogenous ($C_8NH_4^-$, $C_8H_9N_2^+$, $C_9H_8N^+$) and ABS ($C_8H_7SO_3^-$, $C_{17}H_{27}SO_3^-$) material. The exception to this is C_7N^- which maintains intensity through the entire profile similarly to the carbon fragments, showing that small amounts of organic nitrogenous material exists in the lowest, etch-resistant layer.

With each chemical class, a phenomenon is observed whereby smaller, simpler ions extend deeper into the deposit while larger, more complex ions lose intensity earlier. For hydrocarbon and nitrogenous material, the more hydrogenated fragments are closer to the surface which again suggests lower layers possess more PAH/NPAC character. For ABS compounds, $C_{17}H_{27}SO_3^-$ drops rapidly while $C_7H_8SO_3^-$ extends deeper. The nitrogenous material in negative mode ($C_8NH_4^-$, C_7N^-) follows this same pattern, as well as the oxygenates in both positive and negative polarities ($C_{12}H_7O^-$ and $C_{12}H_9O^+$). Like in Needle 1, this indicates a propensity for complex chemistries to break down over time resident in these deposits and form a more amorphous, soot-like material.

3D OrbiSIMS Summary This section has demonstrated the high mass accuracy of 3D OrbiSIMS analysis and its application for unequivocal assignment of the chemistries in two needle samples. The high mass resolving power of the Orbitrap™ analyzer allows for the determination of the elemental composition by accurate mass measurement. Structural elucidation of the generated ions can be achieved by MS/MS analysis, removing the requirement for standard reference materials. Further, depth profiling has provided information on the distribution of these chemistries.

In the needle from China (Needle 1), unique chemical features are zinc, large intensities of calcium salts (in particular sulfates, cyanides, cyanates, hydroxides and phosphates), larger carbon fragments, less hydrogen-rich hydrocarbons (likely related to large PAH-type structures), carboxylates, PDMS and metal ions of iron, chromium, and other common steel alloying metals. The largest intensities observed are calcium salts, carbonaceous material and needle metal substrate. Depth profiling showed a ubiquitous presence of calcium salts and carbon fragments throughout the deposit thickness, both of which steadily decline throughout the profiles. Other, mostly organic, materials reduce in intensity earlier, especially PDMS and palmitate/stearate which fall dramatically at the surface. The ions that extend deeper into the deposit are generally smaller and simpler, likely representing breakdown of material in the deposit at lower depths. Metals could be seen rising in intensity towards the end, representing the needle substrate.

For Needle 2, sourced from Eastern USA, unique features are extremely large intensities of sodium salts (mostly as chlorides, sulfates, cyanides, cyanates, hydroxides and carbonates) and potassium chloride presence. This sample also has large carbon fragment intensities, and its hydrocarbon ions have more hydrogen saturation except for those associated with a lower carbon layer which may be needle substrate related. Profiling also showed a sub-surface spike in sodium salt material that steadily declines towards the final interface and

demonstrated the same effect as in Needle 1 whereby simpler chemistries extend further into the deposit.

XPS Depth Profiling for Elemental Quantification

XPS spectra were recorded with sequential etching using an Ar_{500}^+ GCIB as described in the experimental in the methodology to provide quantification of atomic abundance with depth that complements the semi-quantitative SIMS profiles.

Summed XPS Spectra for Bulk Elemental Quantification The summed XPS spectra (Figure 8) for each profile from 60-1850 s of etching were used to quantify the elements present in each sub-surface bulk deposit. Note that hydrogen cannot be measured with XPS. Regions were assigned for the identifiable elements, and the relative abundance of these elements is shown in Table 2, with substrate-related metals (Fe, Cr and Mo) excluded and the data renormalized to give a closer comparison of the two IDIDs. These metals were only seen in Needle 1's deposit and appear after the first etch (30 s etch time), a reflection of the underlying etch-resistant carbonaceous layer on Needle 2 as discussed with the SIMS depth profiles. Exclusive or vastly more abundant elements in Needle 1's deposit are calcium, zinc, phosphorous and silicon, and in Needle 2 are sodium and chlorine. Other key differences are the larger carbon and nitrogen contents of Needle 2 and larger oxygen content in Needle 1. While salt material is a significant portion of the deposit, the extreme intensity of salt in Needle 2's SIMS data is not a true reflection of the sample, with sodium here only representing 11.1 at% and calcium 0.3 at% while carbon dominates both samples. Similarly, in Needle 1, calcium salts were very intense in the SIMS data but here calcium represents 5.9 at% with sodium only 0.4 at%. Though minor components of the SIMS spectra, here chlorine and potassium are not detected in Needle 1 and 2, respectively. This quantification also provides insight into ABS compounds and sulfate salts, which were significant contributions to the SIMS profiles, however in both samples sulfur represents only 0.4 at%. Zinc shows a significant concentration in Needle 1 (1.6 at%) and hence may be responsible for this injector's fouling (the CEC F-98-08 engine test uses a Zn dosing of only 1 ppm [32]). However, along with sulfur, the concentration of phosphorous (0.1 at%) is very small. Therefore, ZDDP will have undergone breakdown and loss of phosphate. The large share of oxygen in Needle 1 is likely a reflection of etching with this sample having reached the metal of the needle and hence both substrate-related metal oxide and deposit oxygen are part of this data.

FIGURE 8 Summed XPS spectra for etch times 60-1850 s

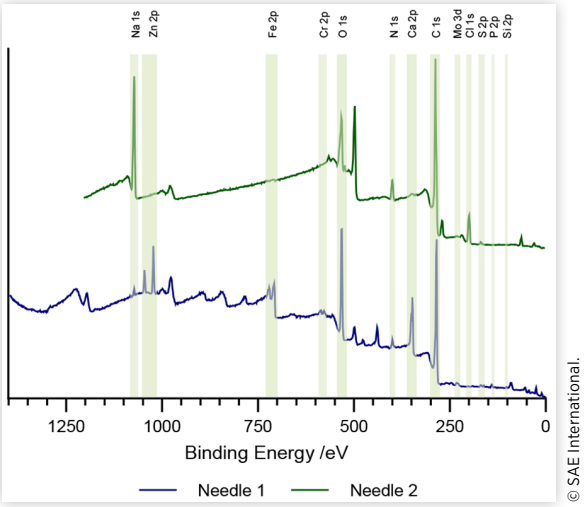

XPS Depth Profiles to Quantify Atomic Distribution

Needle 1 XPS Depth Profile During the full 2725-second (45-minute) XPS etch of Needle 1, a continual increase in the concentration of iron, chromium and molybdenum was observed, from 0% at the surface to a final combined concentration of over 14 at%. In contrast, carbon fell from 76 at% to 56 at%. As this work aims to quantify only the elements in the deposit material, substrate metal oxide content was estimated and removed by modelling it as a component of the high-resolution oxygen 1s spectra. To achieve this, a metal oxide component was fitted as an approximation for substrate metal oxide and a second component was fitted to represent "other," deposit-associated oxygen. The full width at half maximum (FWHM) of the "other" oxygen component was constrained to 2–2.6, and the metal oxide component was constrained with a FWHM of 1–1.5 and a position 2.32 eV lower than this "other" deposit oxygen peak. The fitted data of these two components is seen in Figure 9a for the surface spectrum and 9b for the spectrum after 2725 s of etching, where the metal oxide component has grown substantially from 1.9% to 15.4 %. A 3D plot of the consistent growth of this metal oxide "shoulder" throughout etching is seen in Figure 9c, showing the increase of metal oxide relative to organic oxygen during the profile.

After removing substrate chemistry, the profile (Figure 10) shows a more stable concentration of carbon falling from 76 at% to 68 at% and oxygen which rises from 19 at% to 20 at% at 1825 s before falling to 17 at%. This partially matches the SIMS data, which showed a fall in carbon, hydrocarbons and oxygenates. While these elements remain relatively constant, there is a steady rise in calcium from 0.8 at% to 8 at% at 1825 s, along with small increases in zinc and nitrogen that follow a similar pattern. In SIMS, calcium decreased throughout the profile, and this discrepancy may be an effect of ionizability in SIMS, or of different positions in the sample having different structures. This XPS data implies a changing form of the carbon and oxygen in the deposit with depth as the SIMS profiles indicated that much of the calcium material is in oxygen and nitrogen containing forms (sulfate, hydroxide, cyanide and cyanate). Hence the oxygen and nitrogen at lower layers is present in these salts while in higher layers, where calcium is less concentrated, it must exist in other, organic forms. This further agrees with the SIMS data for nitrogenous and oxygenic organic material which decreases with etch time

FIGURE 9 High resolution XPS spectra of Needle 1's oxygen 1s peak at a) 30 seconds etching, b) 2725 seconds etching, with metal oxide and 'other' oxygen components fitted, and c) the envelope of these components throughout the full 2725 s depth profile

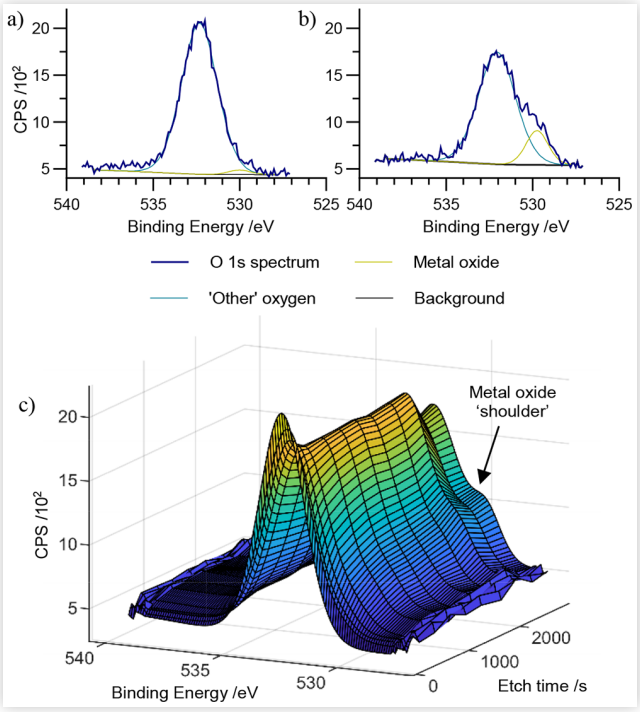

from a maximum intensity at the surface. As carbon remains the most prevalent throughout, this implies that less functionalized organic or amorphous carbon forms these lower layers. Again, the SIMS data supports this as the more complex hydrocarbon material and assignments matching aromatics lost intensity with etching time, while the carbon fragments extended deeper, reaching the metal interface. Finally, silicon demonstrates a rapid decline from 1.5 at% to 0 at% after 9 minutes of etching, evidencing a PDMS surface deposition that agrees with the SIMS data and may be from either a contamination from sample handling or from the fuel.

Needle 2 XPS Depth Profile As seen in the summed spectrum for Needle 2 in Figure 8, no substrate metals are present despite a longer etch time and the darkly colored metal needle being visible in the crater. As with SIMS, this shows the presence of a lower carbon layer. If this is a DLC substrate, then here its data is convoluted with the IDID's carbon data.

An analogous XPS depth profile for 5700 s (1.6 hours) of etching is shown for Needle 2 in Figure 11, in which the change in atomic concentration is more dramatic than in Needle 1. Carbon shows the greatest change, falling from 76 at% at the surface to 52 at% at 860 s (15 minutes) then rising throughout the rest of the profile. Most of the salt-associated elements' profiles mirror carbon's, rising to their peak at 860 s, where sodium is 16 at% and chlorine 6.5 at%. Sulfur reaches its peak of 1.0 at% after the next etch at 1130 s. These elements then decline throughout the rest of the profile while carbon's abundance is restored. This confirms the presence of the subsurface layer of raised sodium salt concentration as seen in SIMS. Oxygen and nitrogen also fall with these salt elements from 860 s onwards, however they are at high concentrations at the surface (16% and 5% respectively) and show a very limited initial rise between 0 and 860 s. The profiles for these elements correspond with the primary constituents of the salt material seen in SIMS (sodium chlorides, cyanides, cyanates, sulfates, hydroxides and carbonates) with the exception of oxygen and nitrogen from 0–860 s, for which the high surface presence and initial flat profiles most likely relate to the presence of organic oxygenic and nitrogenous material seen with corresponding larger surface intensities in the SIMS profiles. Additionally, the SIMS profile for sodium sulfate ions showed constant intensity during this same region while sodium chlorides increase in intensity, hence the rise in sodium would largely not involve oxygen containing anions. A much smaller amount of silicon is seen than on Needle 1,

FIGURE 10 XPS relative atomic percentage depth profile for Needle 1 excluding metal substrate elements and metal oxide component showing a) main elements, and b) trace elements

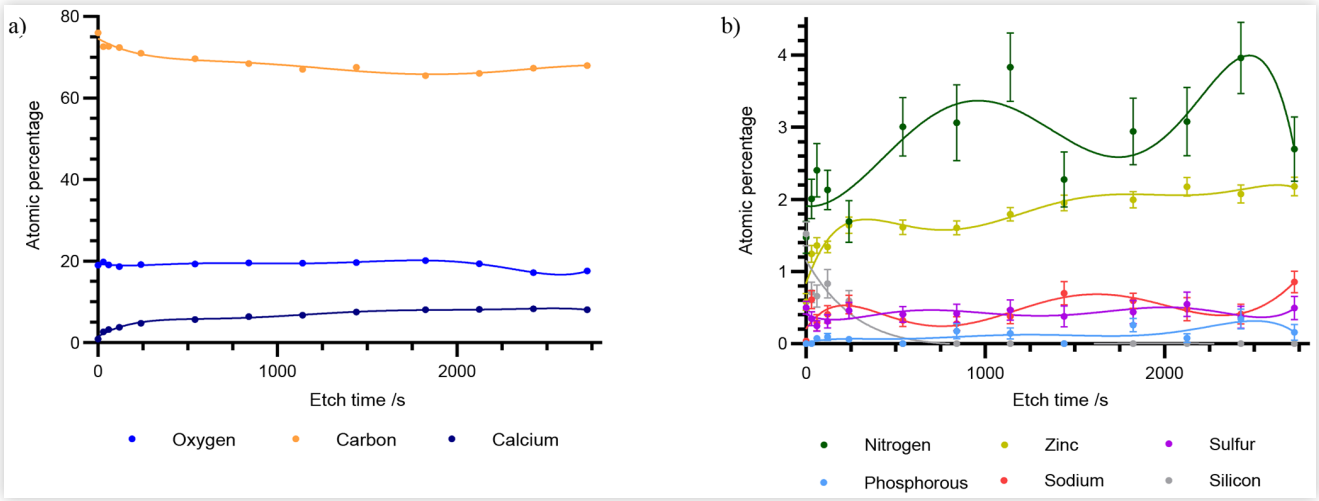

FIGURE 11 XPS relative atomic percentage depth profile for Needle 2 showing a) main elements, and b) trace elements

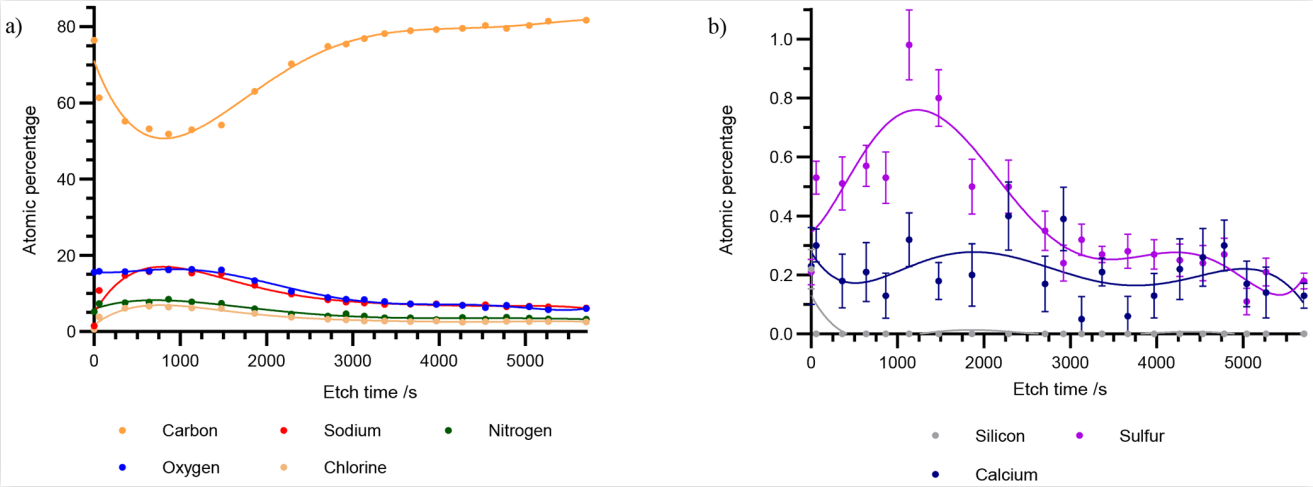

with only 0.2 at% on the pre-etched surface and falling to 0 at% after the first (30 s) etch. This indicates less surface contamination or antifoam deposition on Needle 1. PDMS was not seen in Needle 2's SIMS spectrum despite SIMS being the more sensitive technique, hence silicon's presence here is likely due to differences in composition across the surface.

Similar to Needle 1, the XPS and SIMS results support a more functionalized organic content at the surface containing oxygenated and nitrogenous material. However, in Needle 2 this layer is above a salt layer, beneath which there is likely another carbonaceous layer and finally the etch-resistant carbon layer.

XPS Summary XPS depth profiling has been employed in support of the 3D OrbiSIMS data to quantify the elements both in the sub-surface deposit bulk and throughout the deposit depth profiles. Confirming what was observed in SIMS, zinc, silicon and needle substrate metal elements are seen exclusively in Needle 1, and chlorine in Needle 2. The salt material in both samples was found to have less abundance than was implied by the large intensity peaks in SIMS with carbon remaining the main element at all depths. For Needle 1, substrate-related metal oxides have been modelled and removed from analysis, giving depth profiles of each IDID thickness that validates the general trends in SIMS but demonstrates that carbon remains the predominant element throughout, while calcium gradually increases with depth alongside nitrogen and zinc. The shape of Needle 2's depth profile matches the SIMS profile, where the upper layer has increased concentration of the markers of functionalized organic chemistry (C, N, O), the sub-surface layer has a high concentrations of salt related elements (Na, Cl, S, O, N), and the lower layer is predominantly carbon.

Conclusions

The new method of IDID analysis utilizing 3D OrbiSIMS depth profiling with complementary XPS depth profiling described here provides the ability to probe diagnostic chemistries unambiguously and quantify the relative atomic abundance as a function of depth. The XPS data proves invaluable in order to provide this quantitative contextualization of the semi-quantitative information afforded by 3D OrbiSIMS.

This data reveals new detail in the chemistry of IDIDs, with a deposit model of the needle from China (Needle 1) placing simple hydrocarbon and nitrogenous/oxygenic functionalized organic material in the surface layer, with calcium and zinc rising throughout the deposit thickness indicating a pervasive lubricant oil contamination. Towards the lowermost layers, as oxygen content remains constant while oxygen-containing calcium salt content rises, the carbon that remains the dominant element must therefore exist in less functionalized forms, likely as amorphous soot-like material. The increased PAH content and larger PAH ions in this sample may represent a transitionary stage between fuel and soot-like carbon. For the needle sourced from Eastern USA (Needle 2), the data leads to a model in which functionalized organic chemistry is found more towards the surface, with an underlying layer of heightened salt content that gives way to organic or amorphous carbon material in the bottom layer. If part of this layer is a DLC substrate, it is of note that in this case it did not provide protection from IDID formation.

References

1. Reid, J., and Barker, J., "Understanding Polyisobutylene Succinimides (PIBSI) and Internal Diesel Injector Deposits," SAE Technical Paper 2013-01-2682, 2013, https://doi.org/10.4271/2013-01-2682.
2. Barker, J., Snape, C., and Scurr, D., "Information on the Aromatic Structure of Internal Diesel Injector Deposits from Time of Flight Secondary Ion Mass Spectrometry (ToF-SIMS)," SAE Technical Paper 2014-01-1387, 2014, https://doi.org/10.4271/2014-01-1387.
3. Ullmann, J., Geduldig, M., Stutzenberger, H., Caprotti, R. *et al.*, "Investigation into the Formation and Prevention of

Internal Diesel Injector Deposits," SAE Technical Paper 2008-01-0926, 2008, https://doi.org/10.4271/2008-01-0926.

4. Barker, J., Richards, P., Goodwin, M., and Wooler, J., "Influence of High Injection Pressure on Diesel Fuel Stability: A Study of Resultant Deposits," *SAE Int. J. Fuels Lubr.* 877–884, 2009, https://doi.org/10.4271/2009-01-1877.
5. Banning, M., Barker, J., and Mulqueen, S., "The Nature and Cause of Internal Diesel Injector Deposits and the Effectiveness of Fuel Additives," 28th CIMAC Congress, Helsinki, 2016.
6. Hoang, A.T., and Le, A.T., "A Review on Deposit Formation in the Injector of Diesel Engines Running on Biodiesel," *Energy Sources, Part A* 584–599, 2019, doi:10.1080/15567036.2018.1520342.
7. Alves Fortunato, M., Lenglet, F., Ben Amara, A., and Starck, L., "Are Internal Diesel Injector Deposits (IDID) Mainly Linked to Biofuel Chemical Composition or/and Engine Operation Condition?" SAE Technical Paper 2019-01-0061, 2019, https://doi.org/10.4271/2019-01-0061.
8. de Goede, S., Barbour, R., Velaers, A., Sword, B., *et al.*, "The Effect of Near-Zero Aromatic Fuels on Internal Diesel Injector Deposit Test Methods," *SAE Int. J. Fuels Lubr.*, 163–183, 2017, https://doi.org/10.4271/2017-01-0807.
9. Edney, M.K., Barker, J., Reid, J., Scurr, D.J. *et al.*, "Recent Advances in the Analysis of GDI and Diesel Fuel Injector Deposits," *Fuel*, 2020, doi:10.1016/j.fuel.2020.117682.
10. Dallanegra, R., and Caprotti, R., "Chemical Composition of Ashless Polymeric Internal Diesel Injector Deposits," SAE Technical Paper 2014-01-2728, 2014, https://doi.org/10.4271/2014-01-2728.
11. Cardenas Almena, M.D., Lucio Esperilla, O., Martin Manzanero, F., Murillo Duarte, Y. et al., "Internal Diesel Injector Deposits: Sodium Carboxylates of C12 Succinic Acids and C16 and C18 Fatty Acids," SAE Technical Paper 2012-01-1689, 2012, https://doi.org/10.4271/2012-01-1689.
12. Barker, J., Reid, J., Smith, S.A., Snape, C., et al., "Internal Injector Deposits (IDID)," 11th International Colloquium: Fuels - Conventional and Future Energy for Automobiles, Stuttgart/Osfildern, 2017.
13. Venkataraman, R., and Eser, S., "Characterization of Deposits Formed on Diesel Injectors in Field Test and from Thermal Oxidative Degradation of n-hexadecane in a Laboratory Reactor," *Chem. Cent. J.*, 2008, doi:10.1186/1752-153x-2-25.
14. Trobaugh, C., Burbrink, C., Zha, Y., Whitacre, S. *et al.*, "Internal Diesel Injector Deposits: Theory and Investigations into Organic and Inorganic Based Deposits," *SAE Int. J. Fuels Lubr.* 772–784, 2013, https://doi.org/10.4271/2013-01-2670.
15. Barker, J., Cook, S., and Richards, P., "Sodium Contamination of Diesel Fuel, Its Interaction with Fuel Additives and the Resultant Effects on Filter Plugging and Injector Fouling," *SAE Int. J. Fuels Lubr.* 826–838, 2013, https://doi.org/10.4271/2013-01-2687.
16. Reid, J., Cook, S., and Barker, J., "Internal Injector Deposits from Sodium Sources," *SAE Int. J. Fuels Lubr.* 436–444, 2014, https://doi.org/10.4271/2014-01-1388.
17. Barker, J., Snape, C., and Scurr, D., "A Novel Technique for Investigating the Characteristics and History of Deposits Formed within High Pressure Fuel Injection Equipment," *SAE Int. J. Fuels Lubr.* 1155–1164, 2012, https://doi.org/10.4271/2012-01-1685.
18. Feld, H., and Oberender, N., "Characterization of Damaging Biodiesel Deposits and Biodiesel Samples by Infrared Spectroscopy (ATR-FTIR) and Mass Spectrometry (TOF-SIMS)," *SAE Int. J. Fuels Lubr.* 717–724, 2016, https://doi.org/10.4271/2016-01-9078.
19. Passarelli, M.K., Pirkl, A., Moellers, R., Grinfeld, D. *et al.*, "The 3D OrbiSIMS-Label-Free Metabolic Imaging with Subcellular Lateral Resolution and High Mass-Resolving Power," *Nat. Methods* 1175–1183, 2017, doi:10.1038/nmeth.4504.
20. Edney, M.K., Lamb, J.S., Spanu, M., Smith, E.F., *et al.*, "Unambiguous Identification of Key Molecular Species in Deposits Responsible for Increased Pollution from Internal Combustion Engines," 2020, doi:10.26434/chemrxiv.12666470.v1.
21. XPSFitting, "XPS Reference Pages," www.XPSFitting.com.
22. Omori, T., Tanaka, A., Yamada, K., and Bunne, S., "Biodiesel Deposit Formation Mechanism and Improvement of Fuel Injection Equipment (FIE)," SAE Technical Paper 2011-01-1935, 2011, https://doi.org/10.4271/2011-01-1935.
23. Technical Committee of Petroleum Additive Manufacturers in Europe, 2013, "Fuel Additives: Uses and Benefits.
24. Lacey, P., Gail, S., Kientz, J.M., Milovanovic, N. *et al.*, "Internal Fuel Injector Deposits," *SAE Int. J. Fuels Lubr.* 132–145, 2012, https://doi.org/10.4271/2011-01-1925.
25. da Cunha, A., Sa, A., Mello, S.C., Vasquez-Castro, Y.E., *et al.*, "Determination of Nitrogen-Containing Polycyclic Aromatic Compounds in Diesel and Gas Oil by Reverse-Phase High Performance Liquid Chromatography Using Introduction of Sample as Detergentless Microemulsion," *Fuel*, 119–129, 2016, doi:10.1016/j.fuel.2016.02.035.
26. Taylor, R.S., and Garrison, B.J., "Hydrogen Abstraction Reactions in the Kiloelectronvolt Particle Bombardment of Organic Films," *J. Am. Chem. Soc.* 4465–4466, 1994, doi:10.1021/ja00089a041.
27. Batts, B., and Fathoni, A.Z., "A Literature Review on Fuel Stability Studies with Particular Emphasis on Diesel Oil," *Energy & Fuels* 2–21, 1991, doi:10.1021/ef00025a001.
28. Giakoumis, E.G., and Sarakatsanis, C.K., "A Comparative Assessment of Biodiesel Cetane Number Predictive Correlations Based on Fatty Acid Composition," *Energies*, 2019, doi:10.3390/en12030422.
29. Technical Committee of Petroleum Additive Manufacturers in Europe, 2016, "Lubricant Additives: Use and Benefits.
30. Binkley, R.W., Flechtner, T.W., Tevesz, M.J., Winnik, W. *et al.*, "Rearrangement of Aromatic Sulfonate Anions in the Gas Phase," *Org. Mass Spectrom.* 769–772, 1993, doi:10.1002/oms.1210280708.
31. Stepien, Z., and Krasodomski, W., "Effect of Trace Zinc Amounts Introduced in Various Chemical Structures in Diesel Fuel on Coke Deposits of Fuel Injectors of a CI

Engine," *Int. J. Engine Res.* 755–765, 2020, doi:10.1177/1468087418777175.

32. Barbour, R.H., Quigley, R., and Panesar, A., "Investigations into Fuel Additive Induced Power Gain in the CEC F-98-08 DW10B Injector Fouling Engine Test," SAE Technical Paper Series, 2014, https://doi.org/10.4271/2014-01-2721.

Contact Information

Dr. James Barker
Tel: +44 151 355 3611
jim.barker@Innospecinc.com
Innospec Limited
Innospec Manufacturing Park
Oil Sites Road, Ellesmere Port
Cheshire
CH65 4EY
England
http://www.innospecinc.com

Acknowledgments

This work was funded by the EPSRC Centre for Doctoral Training in Carbon Capture and Cleaner Fossil Energy and Innospec Ltd.. The EPSRC are gratefully acknowledged for the Strategic Equipment grant '3D OrbiSIMS: Label free chemical imaging of materials, cells and tissues' funding that supported this work (grant no. EP/P029868/1). The authors would like to thank Dr. Elisabeth Steer (University of Nottingham) for help with SEM-EDS analysis, Mr. David Knight (Innospec) for disassembling the injectors and Matteo Spanu (University of Nottingham) for code.

Appendix

Appendix 1. Table of Negative Polarity Hybrid SIMS Key Data (Normalized to Total Counts).

Class of Compound	Assignment	Exact Mass	Deviation /ppm	Needle 1 (China) normalized intensity	Needle 2 (Eastern USA) normalized intensity
Calcium salt	$CaO_3H_3^-$	90.9714	N1: -1.9, N2: -2.8	1.23E-04	6.03E-06
	$CaC_3N_3^-$	117.9724	N1: 0.0, N2: -0.9	2.21E-03	7.20E-06
	$CaC_2N_2Cl^-$	126.9381	N1: -0.3, N2: -1.3	4.21E-06	1.09E-04
	$CaC_3N_3O^-$	133.9673	N1: -0.7, N2: -1.2	3.45E-04	5.97E-05
	$CaCNCl_2^-$	135.9039	N1: N/A, N2: -1.6	Noise	7.68E-04
	$CaSO_4H^-$	136.9227	N1: -0.8, N2: -1.6	2.98E-04	1.69E-04
	$CaCl_3^-$	144.8697	N1: N/A, N2: -1.2	Noise	5.47E-03
	$CaSO_4CN^-$	161.9179	N1: -0.5, N2: -1.2	1.57E-05	8.79E-04
	$Ca_2O_5H_5^-$	164.9394	N1: -1.1, N2: -2.4	6.19E-05	1.18E-06
	$Ca_2C_3N_3O_2H_2^-$	191.9404	N1: -0.5, N2: N/A	1.75E-04	Noise
Sodium salt	$NaO_3H_4^-$	75.0064	N1: 2.4, N2: 2.7	3.70E-05	1.49E-06
	$NaC_2N_2O^-$	90.9914	N1: N/A, N2: -2.5	Noise	4.16E-03
	$NaCl_2^-$	92.9280	N1: N/A, N2: -2.6	Noise	2.81E-01
	$NaCNOCl^-$	99.9572	N1: N/A, N2: -1.9	Noise	2.65E-02
	$NaC_2N_2O_2$	106.9863	N1: N/A, N2: -1.0	Noise	4.31E-03
	$NaSO_4$	118.9420	N1: -0.2, N2: -1.2	4.13E-06	8.18E-03
	$Na_2SO_4OH^-$	158.9346	N1: N/A, N2: -1.3	Noise	4.07E-05
	$Na_3SO_4CNCl^-$	225.8934	N1: N/A, N2: -0.6	Noise	1.44E-03
	$Na_3S_2O_8^-$	260.8733	N1: N/A, N2: 0.5	Noise	1.25E-02
	$Na_5S_2O_8Cl_2^-$	376.7906	N1: N/A, N2: -0.6	Noise	1.21E-04
Mixed cation salt	$NaCaSO_4O_2H_2^-$	192.9101	N1: N/A, N2: -1.2	Noise	3.38E-04
	$NaCaS_2O_8^-$	254.8564	N1: 1.4, N2: 0.3	1.61E-06	4.12E-03
Carbon fragment	C_8^-	96.0005	N1: -1.2, N2: -2.3	2.44E-01	6.17E-03
	C_{25}^-	300.0005	N1: -0.1, N2: -0.5	6.46E-04	4.04E-06
	C_{35}^-	420.0005	N1: -0.1, N2: N/A	2.66E-06	Noise
Hydrocarbon (C_xH^-)	$C_{10}H^-$	121.0084	N1: 0.2, N2: -1.3	4.01E-02	2.65E-03
	$C_{14}H^-$	169.0084	N1: -0.6, N2: -1.1	1.22E-02	6.69E-04
	$C_{27}H^-$	325.0084	N1: -0.3, N2: N/A	2.90E-06	Noise

Class of Compound	Assignment	Exact Mass	Deviation /ppm	Needle 1 (China) normalized intensity	Needle 2 (Eastern USA) normalized intensity
Hydrocarbon (C_xH_y)	$C_{13}H_5^-$	161.0397	N1: -0.7, N2: -1.2	3.03E-05	1.42E-05
	$C_{13}H_9^-$	165.0710	N1: -0.8, N2: -1.3	2.30E-06	6.74E-06
	$C_{15}H_5^-$	185.0397	N1: -0.8, N2: -1.2	2.82E-05	5.99E-06
Nitrogenous (C_xN^-)	C_7N^-	98.0036	N1: -1.2, N2: -2.0	3.37E-02	2.09E-03
	$C_{13}N^-$	170.0036	N1: -0.5, N2: 0.3	2.51E-03	2.59E-05
	$C_{14}N^-$	182.0036	N1: -0.6, N2: -0.8	5.73E-04	2.23E-06
	$C_{20}N^-$	254.0036	N1: 1.0, N2: N/A	8.57E-06	Noise
Nitrogenous ($C_xH_yN^-$)	$C_8H_4N^-$	114.0349	N1: 0.0, N2: -1.2	1.16E-04	7.57E-04
	$C_{10}H_6N^-$	140.0506	N1: -0.3, N2: -1.3	3.01E-05	4.23E-04
	$C_{12}H_4N^-$	162.0349	N1: -0.6, N2: -1.2	1.17E-04	2.65E-04
	$C_{14}H_4N^-$	186.0349	N1: -0.7, N2: -1.1	8.85E-05	1.05E-04
	$C_{14}H_8N^-$	190.0662	N1: -0.2, N2: -0.8	4.16E-06	9.66E-05
	$C_{16}NH^-$	207.0114	N1: -0.6, N2: 1.3	2.08E-04	2.67E-06
Nitrogenous ($C_xN_2H_y^-$)	$C_5N_2H^-$	89.0145	N1: -2.5, N2: -3.1	9.88E-05	1.19E-03
	$C_7N_2H^-$	113.0145	N1: 0.2, N2; -0.7	1.66E-04	5.25E-04
Oxygenates ($C_xH_yO^-$)	C_6OH^-	89.0033	N1: -2.5, N2: -3.2	1.16E-04	1.52E-04
	C_8O^-	111.9955	N1: 0.1, N2: -0.4	1.01E-04	9.73E-07
	$C_8H_5O^-$	117.0346	N1: 0.5, N2: -1.0	7.39E-05	2.11E-04
	$C_{12}H_7O^-$	167.0502	N1: -0.5, N2: -1.3	1.71E-05	7.86E-05
Oxygenates ($C_xH_yO_2^-$)	$C_7H_5O_2^-$	121.0295	N1: -0.6, N2: -1.2	1.94E-05	1.21E-04
	$C_9H_5O_2^-$	145.0295	N1: -1.3, N2: -1.4	3.31E-05	9.81E-05
Carboxylates	$C_{16}H_{31}O_2^-$	255.2330	N1: 2.0, N2: N/A	1.30E-05	Noise
	$C_{18}H_{35}O_2^-$	283.2643	N1: 1.3, N2: N/A	1.88E-06	Noise
Alkylbenzene sulfonate	$C_8H_7O^-$	119.0491	N1: 0.3, N2: 1.3	3.12E-04	5.29E-04
	$C_8H_7SO_3^-$	183.0121	N1: -3.1, N2: -1.2	4.51E-04	6.18E-04
	$C_9H_9SO_3^-$	197.0278	N1: 0.2, N2: -0.9	1.64E-05	2.57E-05
	$C_{17}H_{27}SO_3^-$	311.1686	N1: 1.3, N2: -0.1	1.03E-05	3.68E-05
Zinc	ZnO_2^-	95.9195	N1: 0.6, N2: N/A	3.93E-05	Noise
	$ZnSO^-$	111.8967	N1: 0.0, N2: N/A	7.91E-06	Noise
Metal needle substrate	FeO_2^-	87.9253	N1: -2.5, N2: -3.4	6.64E-03	2.63E-05
	VO_3^-	98.9293	N1: 1.2, N2: N/A	1.60E-03	Noise
	CrO_3^-	99.9258	N1: -1.1, N2: -1.5	1.68E-02	8.24E-06
	FeO_3^-	103.9202	N1: -0.3, N2: -1.2	6.95E-03	5.95E-05
	MoO_3^-	145.8907	N1: -0.8, N2: N/A	6.09E-03	Noise
	MoO_4^-	161.8855	N1: -0.7, N2: N/A	3.16E-04	Noise
	WO_5^-	263.9261	N1: 1.2, N2: N/A	4.28E-04	Noise

Appendix 2. Table of Positive Polarity Hybrid SIMS Key Data (Normalized to Total Counts)

Class of Compound	Assignment	Exact mass	Deviation /ppm	Needle 1 (China) normalized intensity	Needle 2 (Eastern USA) normalized intensity
Calcium salt	$CaPO_2^+$	102.9256	N1: -0.1, N2: N/A	2.45E-03	Noise
	$Ca_2O_3H_3^+$	130.9329	N1: -1.2, N2: -1.1	2.09E-01	8.30E-05
	$Ca_2O_4H_5^+$	148.9434	N1: -1.3, N2: -1.5	1.70E-01	4.59E-05
	$Ca_2O_2H_2CNO^+$	155.9281	N1: -2.0, N2: N/A	1.70E-03	Noise
	$Ca_{11}O_{20}H_{19}^+$ H_{19}^+	778.6349	N1: -1.0, N2: N/A	7.24E-05	Noise

Class of Compound	Assignment	Exact mass	Deviation /ppm	Needle 1 (China) normalized intensity	Needle 2 (Eastern USA) normalized intensity
Sodium salt	Na_2Cl^+	80.9478	N1: N/A, N2: 2.6	Noise	3.53E-01
	Na_3S^+	100.9408	N1: N/A, N2: 0.5	Noise	6.65E-03
	$Na_3O_2H_2^+$	102.9742	N1: N/A, N2: 0.2	Noise	7.09E-03
	$Na_3CO_3^+$	128.9535	N1: -1.4, N2: -1.1	8.74E-07	6.33E-03
	Na_3CNCl^+	129.9407	N1: N/A, N2: -1.0	Noise	8.75E-04
	$Na_3Cl_2^+$	138.9065	N1: N/A, N2: -1.3	Noise	1.73E-02
	$Na_3C_2N_2O_2^+$	152.9647	N1: 0.7, N2: -1.6	3.65E-06	8.42E-06
	$Na_3SO_4^+$	164.9205	N1: -1.2, N2: -1.1	1.62E-05	1.32E-01
	$Na_4SO_4CN^+$	213.9133	N1: -1.6, N2: -0.8	4.83E-06	4.72E-04
	$Na_8S_2O_8Cl_3^+$	480.7276	N1: 2.6, N2: 0.1	1.00E-04	4.86E-06
Mixed cation salt	$KNaCl^+$	96.9218	N1: N/A, N2: 0.9	Noise	6.33E-03
	$CaNa_2O_3H_3^+$	136.9498	N1: -1.4, N2: -1.2	6.77E-07	2.80E-04
	$KNa_2SO_4^+$	180.8944	N1: N/A, N2: -1.2	Noise	5.36E-03
	$CaNa_2SO_4OH^+$	198.8961	N1: N/A, N2: -1.2	Noise	1.56E-05
	$CaNa_3SO_4ClOH^+$	256.8547	N1: N/A, N2: -0.7	Noise	2.41E-05
Carbon fragment	C_{11}^+	131.9995	N1: -1.3, N2: -1.4	3.38E-05	4.84E-04
	C_{15}^+	179.9995	N1: -1.3, N2: -1.7	1.37E-05	3.63E-04
	C_{24}^+	287.9992	N1: N/A, N2: -0.9	3.87E-07	2.49E-06
Hydrocarbon	$C_9H_7^+$	115.0542	N1: 0.1, N2: -0.2	1.13E-04	9.44E-04
	$C_{12}H_8^+$	152.0621	N1: -1.2, N2: -1.5	8.19E-05	3.85E-04
	$C_{16}H_{10}^+$	202.0777	N1: -0.7, N2: -1.1	4.11E-05	9.62E-05
	$C_{24}H_{12}^+$	300.0934	N1: -0.3, N2: -0.2	7.32E-06	2.86E-06
	$C_{38}H_{16}^+$	472.1247	N1: 0.6, N2: N/A	1.26E-06	Noise
	$C_{39}H_{15}^+$	483.1168	N1: -0.4, N2: N/A	9.97E-07	Noise
	$C_{41}H_{17}^+$	509.1325	N1: -0.2, N2: N/A	8.97E-07	Noise
	$C_{56}H_{20}^+$	692.1560	N1: -0.3, N2: N/A	8.23E-07	Noise
Nitrogenous ($C_xH_yN^+$)	$C_8H_7N^+$	117.0572	N1: -0.2, N2: -0.4	7.61E-06	1.93E-04
	$C_9H_8N^+$	130.0651	N1: -0.5, N2: -0.9	1.56E-05	2.30E-04
	$C_{10}H_8N^+$	142.0650	N1: -1.0, N2: -1.2	5.50E-06	4.40E-05
	$C_{10}H_9N^+$	143.0730	N1: -1.1, N2: -1.3	7.88E-06	4.32E-05
	$C_{11}H_8N^+$	154.0649	N1: -1.4, N2: -1.6	2.01E-05	1.09E-04
	$C_{12}H_{14}N^+$	172.1121	N1: -1.4, N2: -1.5	1.62E-05	2.41E-06
Nitrogenous ($C_xH_yN_2^+$)	$C_5H_7N_2^+$	95.0604	N1: 1.4, N2: 1.0	1.84E-06	5.72E-04
	$C_5H_9N_2^+$	97.0760	N1: 1.4, N2: 0.8	1.70E-06	2.89E-04
	$C_8H_9N_2^+$	133.0760	N1: -1.1, N2: -1.2	1.64E-06	3.01E-04
	$C_{10}H_7N_2^+$	155.0604	N1: -1.5, N2: -1.7	4.73E-06	1.08E-04
Oxygenates	$C_6H_7O^+$	95.0491	N1: 1.6, N2: 1.1	2.26E-05	3.61E-04
	$C_8H_7O^+$	119.0491	N1: 0.1, N2: -0.3	1.47E-06	1.43E-05
	$C_{10}H_9O^+$	145.0648	N1: -1.1, N2: -1.4	1.42E-05	1.09E-04
	$C_{12}H_8O^+$	168.0570	N1: -1.2, N2: -1.5	1.04E-05	1.23E-05
	$C_{12}H_9O^+$	169.0646	N1: -1.2, N2: -1.5	2.43E-05	9.24E-05
PDMS	$Si_2O_2C_4H_{13}^+$	149.0449	N1: -0.9, N2: N/A	3.70E-06	Noise
Metal needle substrate	$MoO_3H_2^+$	147.9053	N1: -1.9, N2: N/A	3.62E-05	Noise
	$Fe_2O_6H_6^+$	213.8856	N1: -1.0, N2: N/A	6.66E-03	Noise
	$Fe_2O_6H_8^+$	215.9014	N1: -0.6, N2: N/A	4.72E-03	Noise
	$Fe_3O_7H_8^+$	287.8313	N1: -0.9, N2: N/A	2.39E-03	Noise
	$Mo_2O_6H_7^+$	298.8345	N1: 1.5, N2: N/A	1.70E-04	Noise
	$Mo_2O_7H_8^+$	315.8373	N1: -1.6, N2: N/A	5.62E-04	Noise

e-ISSN 2641-9645